Sub-barrier fusion of deformed nuclei in ^{60}Ni+^{154}Sm and ^{32}S+^{182}W reactions

S. Mitsuoka, H. Ikezoe, K. Nishio, and J. Lu
Japan Atomic Energy Research Institute, Tokai, Ibaraki 319-1195, Japan
(Received 5 November 1999; published 3 October 2000)

We have investigated the sub-barrier fusion between spherical projectiles and well-deformed targets in ^{60}Ni+^{154}Sm and ^{32}S+^{182}W reactions, and both lead to the same compound nucleus ^{214}Th. In order to get direct evidence that the projectile really fuses with the deformed target, the fusion evaporation residues emitted to the beam direction were measured by using the JAERI recoil mass separator and identified on the basis of time- and position-correlated α decays. The angular distributions of fission fragments were also measured to obtain the total fusion cross section. The measured cross sections of the fusion fission and the fusion evaporation were compared with the results of the coupled channel calculation and the statistical model calculation, respectively. In the ^{32}S+^{182}W system, a good agreement between them was obtained for xn, pxn, and αxn channels. In the heavy projectile system of ^{60}Ni+^{154}Sm, on the other hand, the observed evaporation residue cross sections below the Bass barrier were much less than the calculated results whereas they were well reproduced above the barrier. It was found that this large hindrance could be reproduced by assuming an extra-extra push energy of around 20 MeV in the tip collision of the deformed target and nearly zero in the side collision.

PACS number(s): 25.70.Gh, 25.70.Jj, 27.80.+w

I. INTRODUCTION

Toward the ''island of stability'' of superheavy elements at or near the predicted double magic nucleus ^{298}114, great efforts have been made to synthesize the superheavies by using the hot-fusion reaction [1] with actinide targets and the cold-fusion reaction [2] with lead-based targets of shell closed spherical nuclei. Very recently, the synthesis of a good candidate for the heaviest elements of 114 [3], 116, and 118 [4] by these reactions has been reported. These types of fusion reaction have been promising to produce such superheavy elements but the production cross sections are of the order of a picobarn or less due to the strong decreasing trend of the cross sections as the atomic number of the synthesized elements increases. As a novel path to the superheavy region by heavy-ion fusion reactions, the gentle fusion [5] and the hugging fusion [6] between well-deformed nuclei have been theoretically proposed. The relative orientation of the symmetry axes of the deformed nuclei significantly changes the Coulomb barrier height and the compactness of the touching configuration. When the symmetry axes are orthogonal to each other at the contact point, the two deformed nuclei can take the most compact configuration. It is predicted that this compact configuration would have a high formation probability of the spherical compound nucleus. Furthermore, it is expected that this touching configuration with the orthogonal symmetry axes would make the fusion path far from the competing axial-symmetric fission path. As a first step to investigate this speculation experimentally, we have measured the fusion cross sections in the reactions of strongly deformed targets ^{154}Sm ($\beta_2=0.32$) and ^{182}W ($\beta_2=0.28$) with spherical projectiles of ^{60}Ni and ^{32}S, respectively.

Heavy-ion fusion cross sections at energies above the Coulomb barrier can be reproduced by the one-dimensional barrier penetration model. On the other hand, below the barrier, the measured cross sections are generally enhanced over the predictions of this model. From the early 1970s, a number of authors investigated the sub-barrier fusion of light spherical projectiles with several deformed targets. In the fusion reactions of ^{16}O with even-even samarium isotopes ^{148,150,152,154}Sm, whose equilibrium ground-state shapes change from spherical to deformed as the mass number increases, Stokstad *et al.* clearly demonstrated an important role of the static deformations on the fusion enhancement [7]. Further analysis in the fusion of more massive projectile ^{40}Ar with various Sn and Sm isotopes by Reisdorf *et al.* [8] indicated that the sub-barrier enhancement is strongly correlated with the static deformations and the dynamical effects of collective vibrations. In an early stage of such investigations, Beringer pointed out the possibility of the distortion of nuclear shape by the long-range Coulomb interaction, that is, the approaching two charged nuclei would be flattened into oblate shapes before they contact [9]. However, the results of dynamical calculations by Wong [10] and several authors [11] indicated that the effect of such nuclear deformability was much smaller than the static nuclear deformation. In addition, the rotation angle of the deformed target nucleus induced by the Coulomb interaction during the approaching process was found also to be small ($3°\sim5°$) [11].

Nowadays it is generally accepted that the static deformations, the couplings to the inelastic excitations of projectile and target, and nucleon transfers are important factors to explain the sub-barrier enhancement of the fusion reaction. Recently, high-quality data of fusion cross sections and more exact coupled channel calculations have been available for several reaction systems. By taking the second derivative of the excitation functions precisely measured in the fusion reactions of ^{16}O with ^{144,148,154}Sm and ^{186}W [12], Leigh *et al.* demonstrated that the fusion barrier distribution thus extracted can be a very sensitive probe of the channel coupling, not only with respect to the dominant effects of static deformations but also with respect to the relatively weak inelastic channels.

In the systems of heavy projectile-target combination, the fusion cross sections are extremely hindered as the product Z_1Z_2 of the atomic numbers of projectile and target increases

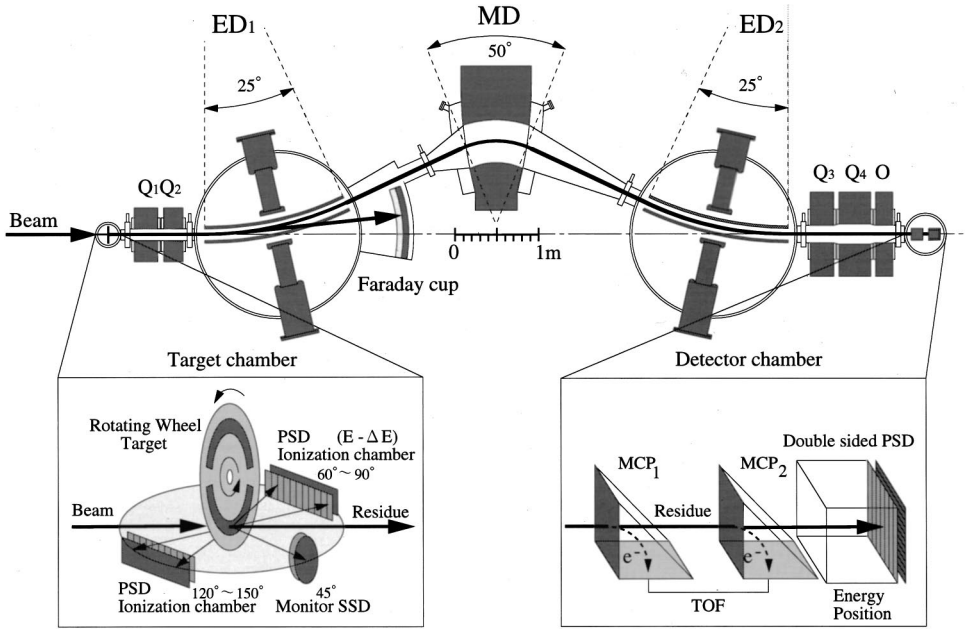

FIG. 1. Schematic layout of the JAERI-RMS (upper part). Magnetic dipole, quadrupole, octupole, and electric dipole are denoted by MD, Q, O, and ED, respectively, with numbers showing the orders of the respective arrangements. Lower parts are the schematic view of the experimental setup at the target position (left side) and the focal plane (right side).

beyond ~1800. This fusion hindrance is known as the extra-push phenomenon, which means that colliding nuclei need an extra kinetic energy to surmount a saddle point of the compound nucleus. We called this energy an *extra-extra push energy* E_{xx}. In the present case of heavy projectile ^{60}Ni with ^{154}Sm, some amount of E_{xx} may be expected because of the large Z_1Z_2 value of 1736. For heavy reaction systems, it has been found that quasifission which proceeds without the formation of a fully equilibrated compound nucleus competes with the fusion-fission. By measuring the fusion barrier distribution and the fission anisotropy in the $^{16}O+^{238}U$ reaction [13], Hinde *et al.* pointed out that the nuclear orientation of the deformed target at the contact point plays an important role in the compound nucleus formation. Especially, they insisted that the collisions with the tips of the deformed nucleus ^{238}U (tip collision) lead to quasifission, while the collisions with the flattened side (side collision) lead to the complete fusion. This suggests that the compact configuration at touching is more favorable for fusion, like the hugging fusion configuration.

In order to get direct evidence that the heavy-ion projectile really fuses with the deformed target, we have measured the fusion-evaporation residues (ER's) in addition to the fission fragments. Because of small ER cross sections down to a few nb level, it is needed to effectively detect a small amount of the ER's in huge backgrounds of the primary beam and other reaction products. For this purpose, we followed a similar technique used to search for superheavy elements [1,2]; the combination of the in-flight separation of ER's by using a recoil mass separator of large solid angle and the identification of ER's by taking advantage of their α-decay properties. In order to extract the effects of the target deformation on the compound nucleus formation, we compared the obtained data with simple model calculations: First the fusion-fission cross sections are compared with the fusion cross section predicted by the coupled channel calculation using the code CCDEF [14]. Here, the fusion cross section is assumed to be approximately equal to the measured fission cross section, since the heavy compound nuclei formed in the present reaction system predominantly undergo fission. And then, the excitation functions of each ER channel are compared to the calculated cross sections by using the statistical model code HIVAP [15]. Here, the parameters used in the HIVAP calculation should be confirmed in the reaction system where no extra-extra push energy is needed. For this purpose, we also have measured the fission and the ER cross sections in the $^{32}S+^{182}W$ reaction, where the same compound nucleus of ^{214}Th is formed as in the $^{60}Ni+^{154}Sm$ reaction. Since the $^{32}S+^{182}W$ system is expected to need no extra-extra push energy because of the sufficiently small value of $Z_1Z_2=1184$, this reaction system was used as a reference to simulate the evaporation process of the compound nucleus ^{214}Th. In this paper, we will discuss how the heavy-ion fusion process depends on the orientation of the deformed target with respect to an angle of incidence of the projectile.

II. EXPERIMENTAL PROCEDURE

The experiments were carried out at the tandem-booster facility of Japan Atomic Energy Research Institute (JAERI). ^{60}Ni and ^{32}S beams of 4–6 MeV/nucleon were used to bombard targets of ^{154}Sm (oxide, 350 μg/cm^2, 98.6% enriched) and ^{182}W (metal, 400 μg/cm^2, 94.5% enriched), respectively. The targets were prepared by sputtering with 30 keV Ar ions onto 0.7 μm aluminum foils. Typical beam intensity from the superconducting booster linac was 10–50 pnA.

A schematic view of the experimental setup is shown in Fig. 1. The target foils were mounted on a rotating wheel of 80 mm in diameter and rotated at 100 rpm. The angular distributions of the fission fragments were measured by two compact $\Delta E-E$ ionization chambers [16], which covered the angular range of $\theta_L=60°-90°$ and $120°-150°$. The Rutherford scattering was monitored at forward angle of θ_L

$=45°$ by a small-area solid-state detector (SSD) for the normalization of the cross section measurements.

The ER's emitted from the target to the beam direction were separated in-flight from the primary beam and various products of background reactions by the JAERI recoil mass separator (RMS) [17]. To provide large angular acceptance (20 msr) and energy acceptance ($\pm 12\%$) of the RMS, the ion-optical parameters were set so that the mass dispersion at the focal plane was zero [18]. As mentioned in Ref. [17], the RMS had been designed especially to reduce a background originating from beam scattering at the anode surface of the first electric dipole ED_1. Consequently the primary beam can pass through the vertical slit of the ED_1 without hitting the anode and be stopped by a large-area Faraday cup located behind the ED_1.

At the focal plane of the RMS, the ER's passed through two thin-foil timing detectors consisting of microchannel plates (MCP's) and were implanted into a double-sided position sensitive strip detector (PSSD, 73 mm $\times$ 55 mm, 15 strips in the front face and 128 strips in the back face). The kinetic energy, the detection time and two-dimensional positions of both the implanted ER and the subsequent α-decay particles were measured. The horizontal and vertical position resolutions were 0.25 mm and 0.5 mm [full width at half maximum (FWHM)], respectively. The energy resolution of the individual front strips was typically 80 keV (FWHM) for 5.486 MeV α particles from an ^{241}Am source. The isotopes of the implanted ER's were identified by the time- and position-correlation analysis of the α-decay events, that is, the implanted ER and the subsequent α decays occurred within the time interval related to their half-lives at the same position within the PSSD resolution. The details of the detection method are shown elsewhere [19].

To obtain the absolute cross sections, we had measured the solid angle and the transmission efficiency of the RMS by using α particles from the source, elastic recoils, and ER's produced in several reactions [18]. The measured efficiency was compared with an ion-optical calculation of the code GIOS [20], and a good agreement between them was obtained. The charge-state distribution of low-energy heavy recoils were also measured [18]. It was found that the empirical formula by Shima *et al.* [21] reproduced well the experimental data. Therefore, we used this formula to estimate the most probable charge state of the ER in a charge-rest carbon foil (30 μg/cm^2) located downstream of the target. The effects of the energy loss and the multiple scattering of ER in the target were estimated by the code TRIM [22]. The energy and the angular distributions for each ER channel were calculated by the statistical model code PACE2 [23]. The total efficiency of the present system was typically 25% for the xn channel and 18% for the αxn channel in the ^{60}Ni $+ ^{154}$Sm reaction.

III. EXPERIMENTAL RESULTS AND ANALYSIS

A. Fusion-fission cross section and CCDEF calculation

Figure 2 shows a typical result of the $\Delta E - E$ measurements obtained in the ^{32}S$+^{182}$W reaction at $E_{\mathrm{c.m.}}=165.5$ MeV ($E_{beam}=195$ MeV) and $\theta_{\mathrm{L}}=62°$. The fission fragments (including both fusion-fission and quasifission) are clearly distinguished from elastic/quasielastic and deep-inelastic scattered particles. The angular distributions of the fission fragments obtained at this energy are shown in Fig. 3. In the transformation from laboratory to center-of-mass system, the symmetric mass division in the fission process was assumed and the total kinetic energy of fission fragments was calculated by the Viola systematics [24]. As shown in Fig. 3, the present angular distributions are well fitted by using a standard formalism for angular distribution of fission fragments as described in Ref. [25], which involves a summation over the spin I of the fissioning system and its projection K on the symmetry axis. In this fitting, the distribution of K value was assumed to be Gaussian with standard deviation K_0^2 which was a fitting parameter. Here, the transmission coefficient $T(I)$ for the partial wave I was calculated by us-

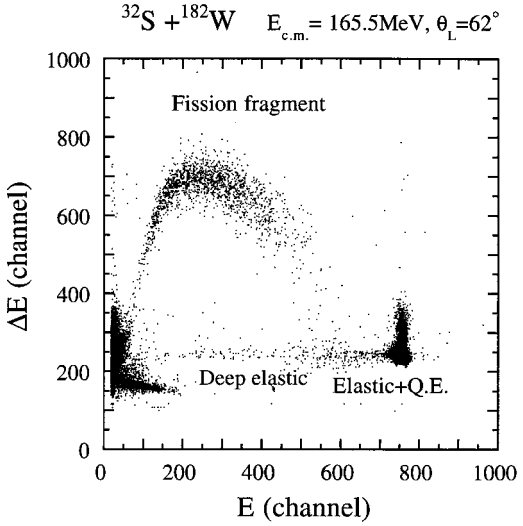

FIG. 2. Two-dimensional matrix of E-ΔE for the ^{32}S$+^{182}$W reaction at $E_{\mathrm{c.m.}}=165.5$ MeV ($E_{beam}=170$ MeV) and $\theta_{\mathrm{L}}=62°$.

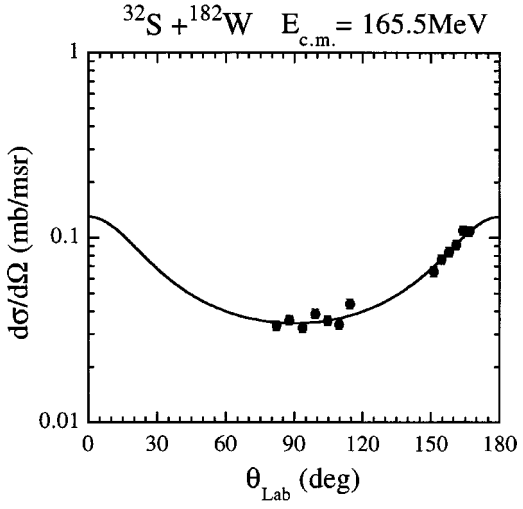

FIG. 3. Angular distribution of fission fragments for the ^{32}S $+^{182}$W reaction at $E_{\mathrm{c.m.}}=165.5$ MeV ($E_{beam}=170$ MeV) and $\theta_{\mathrm{L}}=62°$. Solid curve represents the best fit to the data obtained by varying the K_0^2 parameter.

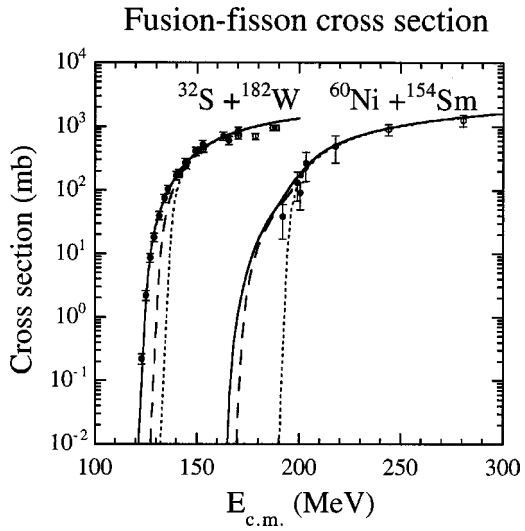

FIG. 4. Experimental fusion-fission cross section in the reactions of ^{32}S+^{182}W (left side), ^{60}Ni+^{154}Sm (right side). The data in Ref. [26] for the same reaction systems are indicated by the open circles. The solid lines are the calculated results of the CCDEF by taking into account the static quadrupole and hexadecapole deformations of the deformed target and the couplings to the inelastic excitations of the low-lying vibrational states of the projectile and the target (see the text). The dotted lines are without the target deformations and the inelastic couplings, and the dashed lines are with the target deformations alone.

ing the CCDEF. The fission cross sections were obtained by integrating the angular distributions of fission fragments thus fitted.

The obtained cross sections both in the ^{32}S+^{182}W and ^{60}Ni+^{154}Sm reactions are shown in Fig. 4 (filled circles) together with the data in Ref. [26] (open circles) for the same reaction systems at higher energies. Since the compound nucleus ^{214}Th formed in the present reaction systems is highly fissible, we assumed that the measured fission cross section is approximately equal to the fusion cross section. In order to calculate the fusion cross section by taking into account the static target deformations and the coupling of the inelastic channels to the fusion process, the coupled channel code CCDEF [14] was used. The dotted lines in Fig. 4 are the calculated results without deformation and coupling, and the dashed lines are with the static target deformations alone. Here, the used parameters of the static quadrupole and hexadecapole deformations are $\beta_2=0.276$ and $\beta_4=-0.089$, respectively, for the ^{182}W target [27], and $\beta_2=0.321$ and $\beta_4=0.08$ for the ^{154}Sm target. The value of β_2 for ^{154}Sm was obtained from the measured quadrupole moment -1.87 barn in Ref. [28].

In the case of ^{32}S+^{182}W, the fusion enhancement observed below the Bass barrier of 136 MeV was not reproduced by the effect of the static deformations alone. By taking the target deformations into account together with the couplings to the inelastic excitations of the low-lying vibrational states 2^+ ($\beta_2=0.312$) and 3^- ($\beta_3=0.485$) for the projectile ^{32}S and 3^- ($\beta_3=0.050$) for the target ^{182}W [29,30], an excellent agreement between the data and the calculated result (solid line) was obtained as shown in Fig. 4. This result indicates that the static deformation and the coupling to the inelastic excitations are equally important to explain the sub-barrier fusion enhancement in the reaction ^{32}S+^{182}W.

In the heavy projectile system of ^{60}Ni+^{154}Sm, the fission measurements could not be extended down to the sub-barrier energy. Below $E_{\mathrm{c.m.}}=190$ MeV, it was experimentally difficult to distinguish the fission fragments unambiguously from the intense background events of the target recoils, quasi- and deep-inelastic products at the forward angles. At the backward angles, the kinetic energy of the fission fragments was too low (5–10 MeV) to be measured by the present detection system. The present data were compared with the CCDEF calculation only above the barrier region $E_{\mathrm{c.m.}}\geqslant 190$ MeV, where the fusion cross section was well reproduced by the CCDEF calculation. Below the barrier region, a large enhancement due to the static deformation of ^{154}Sm was predicted. Gomes *et al.* [31] measured the fusion cross sections of the ^{154}Sm target with the various projectiles of ^{4}He, ^{12}C, ^{16}O, ^{32}S, and ^{40}Ar at sub-barrier energy regions and found that the static deformation of the ^{154}Sm is the main cause responsible for the fusion enhancement, but the best fit of the fusion cross sections was achieved when considering, in addition to the deformation, the coupling to the first 3^- state of the ^{154}Sm and the first 2^+ state of the projectile. The importance of the static deformation of the ^{154}Sm nucleus on the sub-barrier fusion enhancement was also clearly demonstrated by Ref. [32], where the barrier distribution was reproduced well by the coupled channel calculations including the quadrupole and hexadecapole deformations of the ^{154}Sm. According to these results, we took into account the deformation of ^{154}Sm and the inelastic couplings of 2^+ ($\beta_2=0.207$) [29] and 3^- ($\beta_3=0.208$) [30] for ^{60}Ni and 3^- ($\beta_3=0.084$) [30] for ^{154}Sm. The effect of an additional coupling to the higher vibrational states of 2^+ (1.178 MeV) and 2^+ (1.44 MeV) of ^{154}Sm was very weak. The calculated result (solid line) is shown in Fig. 4. This calculated fusion cross section was used to estimate the ER cross sections in the HIVAP calculation.

B. Evaporation residue cross section and HIVAP calculation

As mentioned in the previous section, the ER's separated by the RMS were implanted into the PSSD, which was used to measure their kinetic energies and two-dimensional positions. Before the implantation, the ER's passed through the two timing detectors to obtain the time-of-flight (TOF) information. Figure 5 shows a typical two-dimensional matrix between the energy and the TOF of the incoming particles in the reaction of ^{60}Ni+^{154}Sm at $E_{\mathrm{c.m.}}=200$ MeV ($E_{beam}=291$ MeV). The ER's were clearly separated from a large amount of scattered particles passing through the RMS. The total event rate was about a few cps (counts per second).

Since the ER evaporated from the present compound nucleus ^{214}Th, through xn, pxn, and αxn channels ($x\sim 0$ to 4) has an α-decay branching ratio of nearly 100%, the PSSD signals associated without the TOF signal are considered to originate from the subsequent α decays of the implanted ER's. Figure 6 shows a typical example measured in the

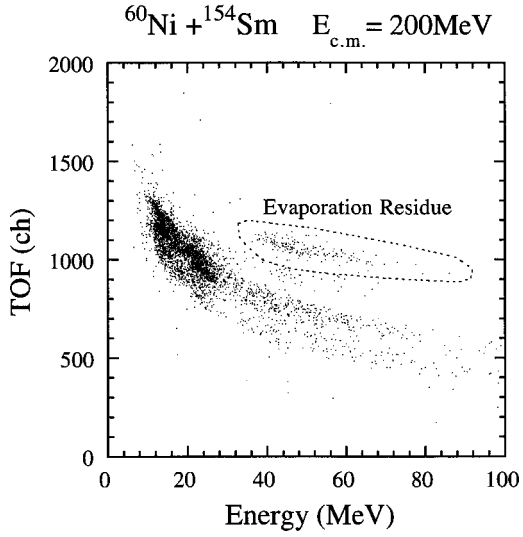

FIG. 5. Two-dimensional matrix between the energy and the TOF of the incoming particles in the reaction of ^{60}Ni+^{154}Sm at $E_{\mathrm{c.m.}}=200$ MeV ($E_{beam}=291$ MeV). Events enclosed by the dashed curve originate from the evaporation residue.

^{60}Ni+^{154}Sm reaction at $E_{\mathrm{c.m.}}=200$ MeV; Fig. 6(a) is the single energy spectrum of the α-decay particles and Fig. 6(b) is the two-dimensional spectrum of the energy E_α versus the detected time interval ΔT ($\leqslant$500 s) between the α-decay particle and the position-correlated ER, whose position difference was within $\Delta X=\Delta Y=0.5$ mm. The identification of each evaporation channel was performed on the basis of the α-decay properties (α-decay energy $E_{\alpha 1}$ and lifetime τ) of the ER$-\alpha_1$ decay chain. The boxes in Fig. 6(b) indicate the eyes guide for each α-decay property having appropriate energy width of $\pm$50 keV and $\frac{1}{10}\tau\leqslant\Delta T\leqslant 10\tau$. Since the decay properties for some pairs of isotopes (e.g., ^{212}Th and ^{211}Th, ^{211}Ac and ^{210}Ac, and so on) are very similar to each other, the definite identification between them was not achieved. Some events observed uniformly around $\Delta T=100\sim500$ s are chance coincidence with the backgrounds. The ER identifications were confirmed by the correlated $\alpha_1-\alpha_2$ chains between the parent and the daughter α decays as shown in Fig. 6(c). For example, the identified ER$-\alpha_1$ events of 19 for ^{210,211}Ac is consistent with the observed ten events of the $\alpha_1-\alpha_2$ chain, because half of the α-decay events were considered to escape from the PSSD without depositing its full energy. For the other cases, consistency is also obtained; e.g., the identified events 37 for ^{206,207}Fr consist of the six events of the $\alpha_1-\alpha_2$ correlations since the daughter nuclei ^{202,203}At has an α-decay branching ratio of less than 30%. We could estimate the ER's directly produced by αxn and αpxn channels separately from the daughter nuclei of ER's produced by xn and pxn channels. In order to obtain the cross sections of αxn and αpxn channels, the counts of αxn and αpxn channels were subtracted from those of xn and pxn channels, respectively, corresponding to their parent nuclei.

The ER cross sections thus obtained for xn, pxn, αxn, and αpxn channels are shown in Figs. 7 and 8 in the reactions of ^{32}S+^{182}W and ^{60}Ni+^{154}Sm, respectively. The error

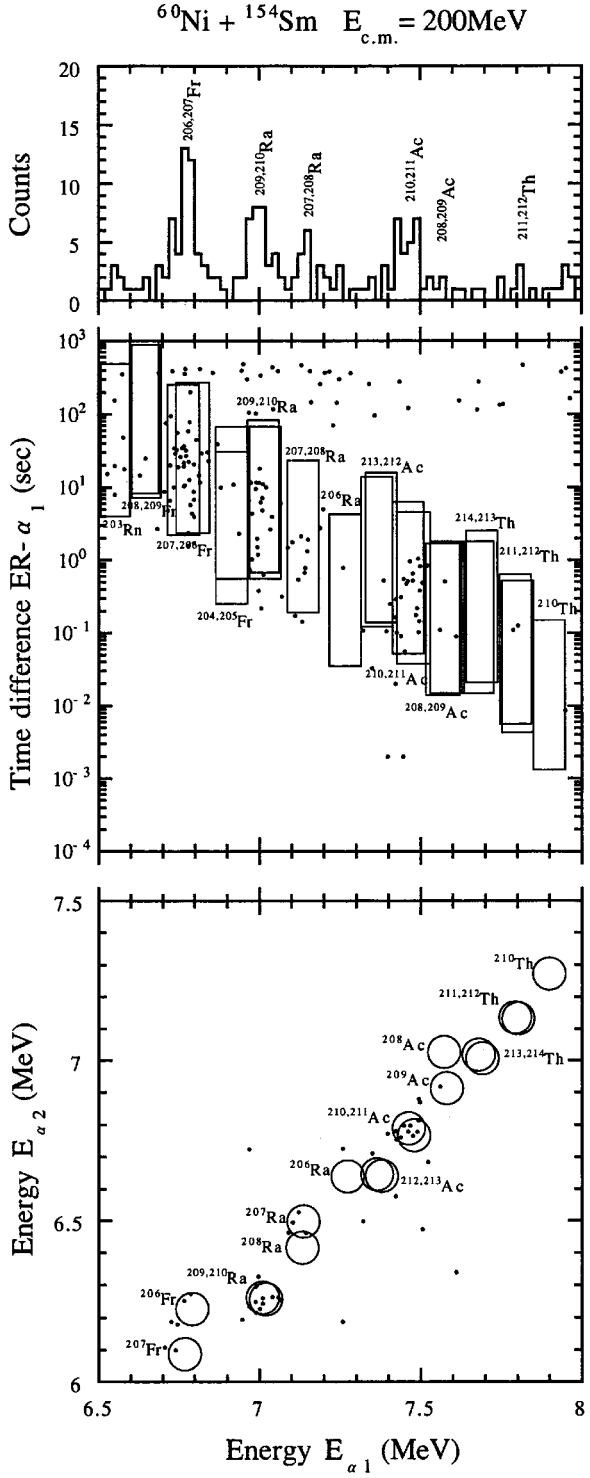

FIG. 6. Measured spectra of the energy E_α in the ^{60}Ni+^{154}Sm reaction at $E_{\mathrm{c.m.}}=200$ MeV ($E_{beam}=291$ MeV). (a) Single energy spectrum of the α-decay particles without the TOF signal. (b) Two-dimensional spectrum of the energy versus the detected time interval within $\Delta T=500$ s between the α-decay particle and the position-correlated ER, whose position difference was within $\Delta X=\Delta Y=0.5$ mm. (c) Two-dimensional matrix showing the correlation between parent and daughter α decays of $\alpha_1-\alpha_2$ chain. Boxes in (b) and circles in (c) are guides for the eyes for each α-decay property of decay energy E_α and lifetime τ ($E_\alpha-50$ keV$\leqslant E\leqslant E_\alpha+50$ keV, $\frac{1}{10}\tau\leqslant\Delta T\leqslant 10\tau$).

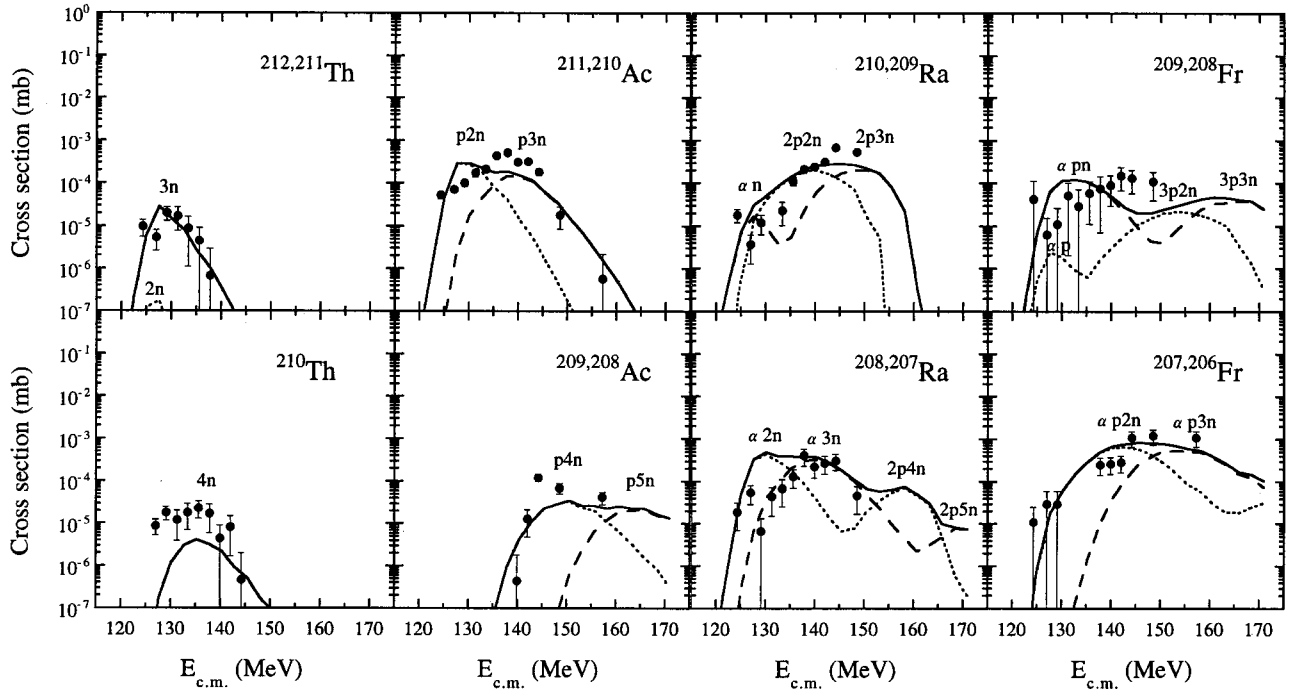

FIG. 7. Measured ER cross sections in the $^{32}S+^{182}W$ reaction. The solid curves show the calculated results of HIVAP. The dotted and dashed curves are for the individual ER component. Each evaporation channel is shown on each corresponding curve.

includes the statistical one in addition to the systematic error of 40% for the estimations of the RMS transmission and the angular distribution of the ER's. We compared the obtained data with a statistical model calculation using the code HIVAP [15]. In this calculation, the level density parameter a_n and a_f at the ground-state deformation and the saddle-point deformation, respectively, were assumed to be

$$a=\tilde{a}\{1+[1-\exp(-E/18)]E_s/E\}, \tag{1}$$

where the asymptotic value of $\tilde{a}$ was calculated as given in Ref. [33]

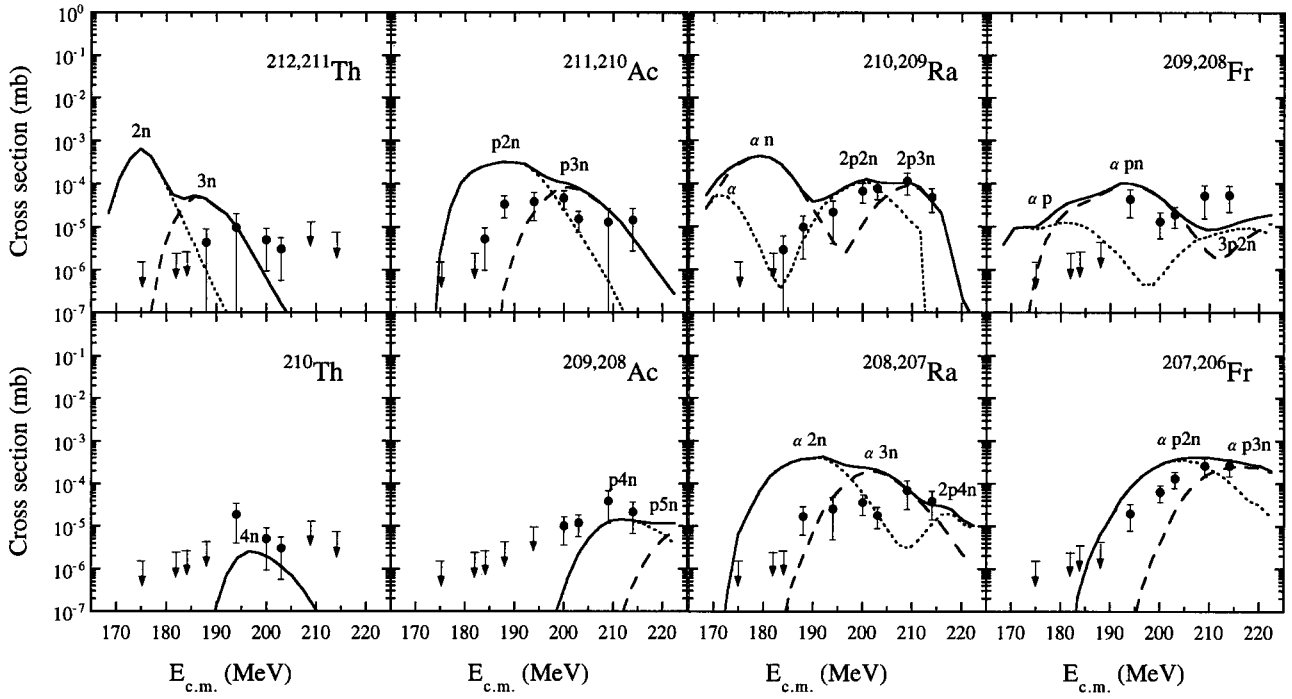

FIG. 8. Same as Fig. 7 except for the $^{60}Ni+^{154}Sm$ reaction. The solid curves are the calculated results of HIVAP. The dotted and dashed curves are for the individual ER component. Each evaporation channel is shown on each corresponding curve.

$$\tilde{a} = 0.069A + 0.165A^{2/3}B_s + 0.175A^{1/3}B_k . \quad (2)$$

The shape dependences B_s and B_k are defined in Ref. [34]. E_s is a shell correction energy and E is an excitation energy. Here the shell damping factor of 18 MeV was used [35]. The shell correction energy was obtained as the difference of the experimental mass taken from Ref. [36] and the liquid drop mass [37]. According to Refs. [38,39], the rotational and vibrational enhancements of the level density $\rho(E)$ was taken into account:

$$\rho(E) = K_{rot}K_{vib}\rho_{int}(E), \quad (3)$$

where K_{rot} and K_{vib} are the coefficients for rotational and vibrational enhancements of noncollective internal nuclear excitations $\rho_{int}(E)$. In this calculation, the ground-state quadrupole deformation β_2 was taken from Ref. [40], while the saddle-point deformation was taken from Ref. [41]. The fission barrier height B_f was given as $B_f = B_{LD} - E_s$, where the liquid drop fission barrier B_{LD} was calculated by Ref. [41].

The solid lines in Fig. 7 shows the calculated results for the $^{32}S + ^{182}W$ reaction, and the dotted and dashed lines indicate those of each ER channel. For all ER channels, good agreement between the data and the calculated results was obtained without any hindrance as we expected. In the $^{60}Ni + ^{154}Sm$ reaction, however, as shown in Fig. 8, the observed ER's cross sections were considerably smaller than the calculated results (the solid lines) at the low-energy region of $E_{c.m.} = 180-200$ MeV, while a reasonable agreement is shown at the higher energy region. Here, the Bass barrier in this system is 192.8 MeV. It is remarkable that no event was observed at $E_{c.m.} = 175$ and 182 MeV in the contrast with the calculations for the ER corresponding to the $2n$, α, and αp channels. The upper limits of the cross section at each $E_{c.m.}$ were determined as 1 event counting the yield indicated by the arrows in the figure. The hindrance factor of the measured ER cross section at these low-energy regions is about 10^2-10^3.

IV. DISCUSSION

As shown above, for both the fusion-fission and ER cross sections, good agreement between the data and the calculated results was obtained in the lighter projectile system of $^{32}S + ^{182}W$. In contrast, in the heavier projectile system of $^{60}Ni + ^{154}Sm$ a large hindrance of the ER cross sections was observed below the Bass barrier, whereas no hindrance was observed above the barrier. These facts can be related to the nuclear orientation of the deformed target at the contact point.

Before going into this discussion, we estimated the net rotation angle of the deformed ^{154}Sm target until the ^{60}Ni projectile comes to the closest distance by the Coulomb interaction. The probability of the Coulomb excitation of the ^{154}Sm nucleus by the ^{60}Ni projectile was calculated by using a code developed by Winther and de Boer [42]. In this calculation, the $E2$ transition up to $I = 12^+$ of ^{154}Sm was assumed and the corresponding $E2$ matrix elements were input in the code, where the $B(E2)$ values were taken from Ref. [43] and the quadrupole moment -1.87 barn [28] of the first excited state ($I = 2^+$) was used. After the excitation probabilities of the rotational ground states of ^{154}Sm were calculated as a function of time, the time-integrated rotation angle of ^{154}Sm up to the closest approach was obtained by using the moment of inertia $J/\hbar = 2.41 \times 10^{-20}$ s. The calculated rotation angle was $2-5$ degrees at the bombarding energy of $E_{c.m.} = 190-220$ MeV and various scattering angles. This rotation angle is somewhat overestimated at the bombarding energy above the Coulomb barrier because the nuclear attractive force was neglected. As mentioned previously, the effect of the distortion of the nuclear shape due to the Coulomb force during the collision had been discussed by several authors [10,11] to be much smaller than the static deformation. In the following discussion, we neglected the small effects of both the rotation and the deformability of the deformed target induced by the Coulomb interaction before the collision.

The Coulomb barrier height in the present system of $^{60}Ni + ^{154}Sm$ is 172 MeV at the tip collision and 198 MeV at the side collision. Although the barrier distribution becomes wider due to the additional inelastic couplings (which effects are minor but important), it is considered that the ER yields at $E_{c.m.} \sim 180$ MeV mainly come from the near-tip collisions. The fact that no ER was observed at $E_{c.m.} = 175$ and 182 MeV suggests that the fusion probability is significantly small at the near-tip collision below the Bass barrier. On the contrary, no fusion hindrance was observed at energy higher than $E_{c.m.} \sim 200$ MeV. Though the collisions for all target orientations occur in the above-barrier energies, it is considered that the near-side collisions mainly contribute to the compound nucleus formation because of their larger solid angle than that of the tip collision. These facts suggest that the near-tip collision needs some extra kinetic energy to become fused, while the side collision leads to complete fusion without such extra energy.

In order to confirm this consideration, we recalculated the ER cross sections by assuming that extra-extra push energy E_{xx} may be needed depending on the colliding angle θ of ^{60}Ni projectile with respect to the orientation of the symmetric axis of the deformed ^{154}Sm target. As mentioned above, the barrier height becomes minimum around $E_{c.m.} \sim 180$ MeV in the tip collision ($\theta = 0°$) and maximum around $E_{c.m.} \sim 200$ MeV in the side collision ($\theta = 90°$). Hence, we properly modified the fusion barrier by adding E_{xx} of 20 MeV to the original barrier height at the tip collision and zero E_{xx} at the side collision, namely $E_{xx} = 20(1 - \theta/90°)$ MeV. The calculated results are shown by the solid lines in Fig. 9, together with the results using the original barrier height (dotted lines). The fact that the solid lines could reasonably reproduce the fusion hindrance below the Bass barrier would support our simple consideration, that is, larger E_{xx} is needed at the tip collisions than that at the side collisions.

It is worth relating this consideration to the distance R/R_0 between the mass centers of the colliding nuclei at the barrier position, where R_0 is the radius of the compound nucleus. In the tip collision of the present $^{60}Ni + ^{154}Sm$ system, the distance $R/R_0 = 1.99$ is longer than the saddle position of 1.83

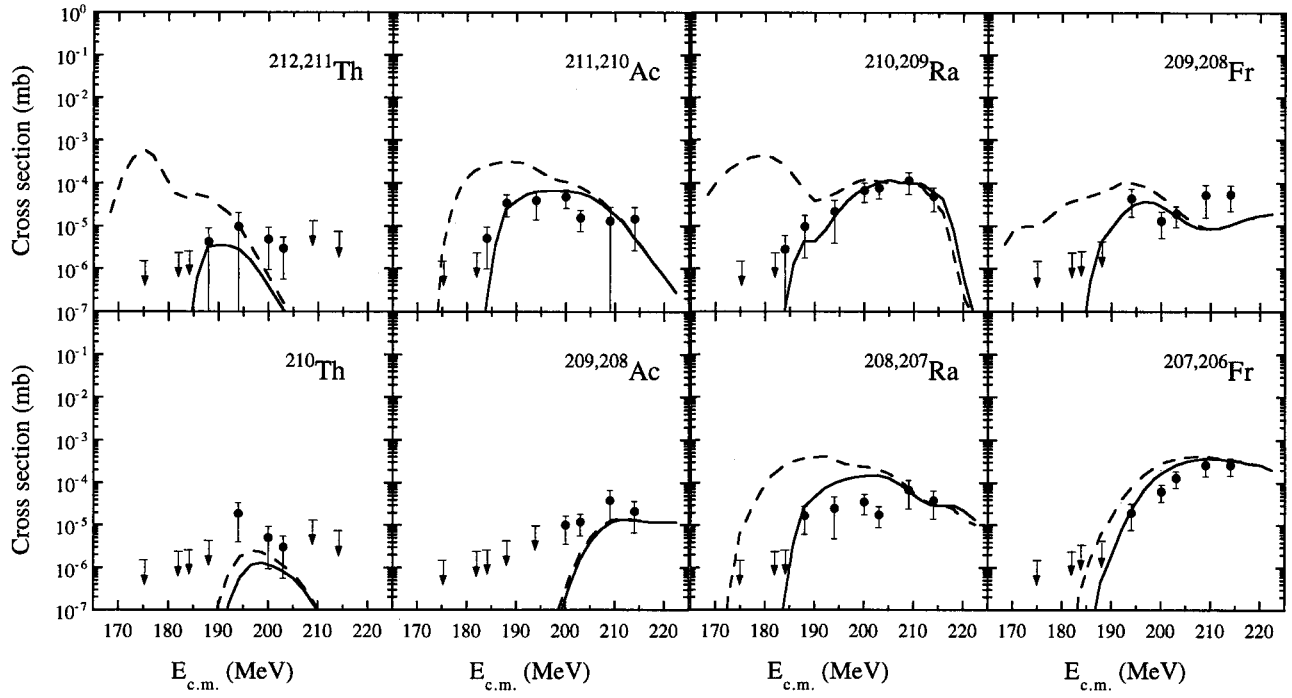

FIG. 9. Same as Fig. 8. The solid curves show the calculated results taking into account the extra-extra push energy (see the text for the details), and the dashed curves are without any extra-extra push energy (the same curves as the solid ones in Fig. 8).

[41], thus extra energy is needed to surmount the saddle point of the compound nucleus. On the other hand, the side collision, where the mass center ($R/R_0=1.64$) is inside the saddle point, would lead to complete fusion without any extra energy if the incident energy is above the fusion barrier. This supports the original speculation that the compact touching configuration leads to the formation of the compound nucleus more easily than an elongated configuration. In the case of the $^{32}S+^{182}W$ system, the fusion can occur irrespective of the touching configuration, because the distance of mass centers is smaller than the position of the saddle point even in the tip collision ($R/R_0=1.75$).

V. SUMMARY AND CONCLUSION

We have measured the fusion-fission and fusion evaporation residue cross sections in the $^{60}Ni+^{154}Sm$ and $^{32}S+^{182}W$ reactions at the sub-barrier energy region. The measured cross sections were compared with the coupled channel calculation for the fusion process (entrance channel) and the statistical model calculation for the evaporation process (exit channel). In the light projectile system of $^{32}S+^{182}W$, a good agreement between the data and the calculated results was obtained both for the entrance channel and for the exit xn, pxn and αxn evaporation channels. In the case of the heavy projectile system $^{60}Ni+^{154}Sm$, even though the same parameter setting with $^{32}S+^{182}W$ was used in the calculation for the deexcitation from the same compound nucleus ^{214}Th, a large discrepancy was observed below the Bass barrier; the measured ER cross sections for all evaporation channels were much less than the calculated results. The hindrance factor was about 10^2-10^3, while no hindrance was observed above the barrier. This sub-barrier fusion hindrance was investigated by relating the colliding angle θ of ^{60}Ni projectile with respect to the orientation of the symmetric axis of the deformed ^{154}Sm target at the contact point. In the tip collisions ($\theta=0°$), some extra kinetic energy to surmount the saddle point would be needed because the distance between the mass centers of the colliding nuclei is longer than the saddle position of the compound nucleus, while the side collision ($\theta=90°$) which is inside the saddle would lead to complete fusion without any extra energy. By assuming that extra-extra push energy E_{xx} is around 20 MeV in the near-tip collisions and zero in the near-side collisions, the measured excitation functions of the ER channels were well reproduced. The present result is consistent with the conclusion obtained by Hinde *et al.*; the side collisions lead to fusion-fission whereas the tip collisions undergo quasifission without forming the fully equilibrated compound nucleus. These facts suggest that it is of importance for the compound nucleus formation to take more compact configuration in the side collision than an elongated shape in the tip collision, as proposed in the original idea of the hugging fusion. In order to confirm the present conclusion, further experimental studies and more realistic calculations of the fusion dynamics between deformed nuclei should be carried out at the sub-barrier region.

ACKNOWLEDGMENTS

The authors thank the crew of the JAERI tandem-booster facility for the operation of beams, and thank Dr. Hojyo and staff for use of their sputter ion source for the target preparation.

[1] Y.A. Lazarev *et al.*, Phys. Rev. Lett. **73**, 624 (1994); **75**, 1903 (1995); Phys. Rev. C **54**, 620 (1996).
[2] S. Hofmann *et al.*, Z. Phys. A **350**, 277 (1995); **350**, 281 (1995); **354**, 229 (1996).
[3] Y.T. Oganessian *et al.*, Phys. Rev. Lett. **83**, 3154 (1999).
[4] V. Ninov *et al.*, Phys. Rev. Lett. **83**, 1104 (1999).
[5] W. Nörenberg, Proceedings of the International Workshop on Heavy-Ion Fusion, Padva, Italy (1994).
[6] A. Iwamoto, P. Möller, J.R. Nix, and H. Sagawa, Nucl. Phys. **A596**, 329 (1996).
[7] R.G. Stokstad, Y. Eisen, S. Kaplanis, D. Pelte, U. Smilansky, and I. Tserruya, Phys. Rev. C **21**, 2427 (1980); R.G. Stokstad and E.E. Gross, *ibid.* **23**, 281 (1981).
[8] R.G. Stokstad, W. Reisdorf, K.D. Hildenbrand, J.V. Kratz, G. Wirth, R. Lucas, and J. Poitou, Z. Phys. A **295**, 269 (1980); W. Reisdorf, F.P. Hessberger, K.D. Hildenbrand, S. Hofmann, G. Münzenberg, K.-H. Schmidt, J.H.R. Schneider, W.F.W. Schneider, K. Sümmerer, G. Wirth, J.V. Kratz, and K. Schlitt, Nucl. Phys. **A438**, 212 (1985).
[9] R. Beringer, Phys. Rev. Lett. **18**, 1006 (1967).
[10] C.Y. Wong, Phys. Lett. **26B**, 120 (1968).
[11] L. Wilets, E. Guth, and J.S. Tenn, Phys. Rev. **156**, 1349 (1967); H. Holm, W. Scheid, and W. Greiner, Phys. Lett. **29B**, 473 (1969); H. Holm and W. Greiner, Phys. Rev. Lett. **24**, 404 (1970); A.S. Jensen and C.W. Wong, Phys. Rev. C **1**, 1321 (1970); P.W. Riesenfeldt and T.D. Thomas, *ibid.* **2**, 711 (1970).
[12] J.R. Leigh, M. Dasgupta, D.J. Hinde, J.C. Mein, C.R. Morton, R.C. Lemmon, J.O. Newton, H. Timmers, J.X. Wei, and N. Rowley, Phys. Rev. C **52**, 3151 (1995).
[13] D.J. Hinde, M. Dasgupta, J.R. Leigh, J.C. Mein, C.R. Morton, J.O. Newton, and H. Timmers, Phys. Rev. C **53**, 1290 (1996).
[14] J. Fernandez-Niello, C.H. Dasso, and S. Landowne, Comput. Phys. Commun. **54**, 409 (1989).
[15] W. Reisdorf and M. Schädel, Z. Phys. A **343**, 47 (1992).
[16] K. Nishio, J. Lu, H. Ikezoe, and S. Mitsuoka, JAERI Tandem & V.D.G Annual Report 1998.
[17] H. Ikezoe, Y. Nagame, T. Ikuta, S. Hamada, I. Nishinaka, and T. Ohtsuki, Nucl. Instrum. Methods Phys. Res. A **376**, 420 (1996).
[18] T. Kuzumaki, H. Ikezoe, S. Mitsuoka, T. Ikuta, S. Hamada, Y. Nagame, I. Nishinaka, and O. Hashimoto, Nucl. Instrum. Methods Phys. Res. A **437**, 107 (1999).
[19] S. Mitsuoka, H. Ikezoe, T. Ikuta, Y. Nagame, K. Tsukada, I. Nishinaka, Y. Oura, and Y.L. Zhao, Phys. Rev. C **55**, 1555 (1997); H. Ikezoe, T. Ikuta, S. Hamada, Y. Nagame, I. Nishinaka, K. Tsukada, Y. Oura, and T. Ohtsuki, *ibid.* **54**, 2043 (1996).
[20] H. Wollnik, a program for the design of general ion-optical system, Physikalisches Insitut, Universitát Giessen, D-6300 Giessen, Germany.
[21] K. Shima, T. Ishihara, and T. Mikumo, Nucl. Instrum. Methods Phys. Res. **200**, 605 (1982); K. Shima, N. Kuno, and M. Yamanouchi, Phys. Rev. A **40**, 3557 (1989).
[22] J.F. Ziegler, J.P. Biersack, and U. Littmark. *The Stopping and Range of Ions in Solids* (Pergamon, New York, 1985).
[23] A. Gavron, Phys. Rev. C **21**, 230 (1980).
[24] V.E. Viola, K. Kwiatkowski, and M. Walker, Phys. Rev. C **31**, 1550 (1985).
[25] R. Vandenbosch and J.R. Huizenga, *Nuclear Fission* (Academic, New York, 1973), p. 179.
[26] B.B. Back, P.B. Fernandez, B.G. Glagola, D. Henderson, S. Kaufman, J.G. Keller, S.J. Sanders, F. Videbæk, T.F. Wang, and B. D. Wilkins, Phys. Rev. C **53**, 1734 (1996).
[27] I.Y. Lee, J.X. Saladin, F.K. McGowan, W.T. Milner, J.L.C. Ford, Jr., R.L. Robinson, and W. Tuffle, Phys. Rev. C **12**, 1483 (1975).
[28] P. Raghavan, At. Data Nucl. Data Tables **42**, 189 (1989).
[29] S. Raman, C.H. Malarkey, W.T. Milner, C.W. Nestro, Jr., and P.H. Stelson, At. Data Nucl. Data Tables **36**, 1 (1987).
[30] R.H. Spear, At. Data Nucl. Data Tables **42**, 55 (1989).
[31] P.R.S. Gomes *et al.*, Phys. Rev. C **49**, 245 (1994).
[32] R.C. Lemmon, J.R. Leigh, J.X. Wei, C.R. Morton, D.J. Hinde, J.O. Newton, M. Dasgupta, and N. Rowley, Phys. Lett. B **316**, 32 (1993).
[33] W. Reisdorf, Z. Phys. A **300**, 227 (1981).
[34] W.D. Myers and W.J. Swiatecki, Ann. Phys. (N.Y.) **84**, 186 (1974).
[35] A.V. Ignatyuk, G.N. Smirenkin, and A.S. Tishin, Yad. Fiz. **21**, 485 (1975) [Sov. J. Nucl. Phys. **21**, 255 (1975)].
[36] G. Audi and A.H. Wapstra, Nucl. Phys. **A595**, 409 (1995).
[37] W.D. Myers and W.J. Swiatecki, Ark. Fys. **36**, 343 (1967).
[38] A.R. Junghans, M. de Jong, H.-G. Clerc, A.V. Ignatyuk, G.A. Kudyaev, and K.-H. Schmidt, Nucl. Phys. **A629**, 635 (1998).
[39] A.S. Iljinov, M.V. Mebel, N. Bianchi, E. de Sanctis, C. Guaraldo, V. Luchierini, V. Muccifora, E. Polli, A.R. Reolon, and P. Rossi, Nucl. Phys. **A543**, 517 (1992).
[40] P. Möller, J.R. Nix, W.D. Myers, and W.J. Swiatecki, At. Data Nucl. Data Tables **59**, 185 (1995).
[41] S. Cohen, F. Plasil, and W.J. Swiatecki, Ann. Phys. (N.Y.) **82**, 557 (1974).
[42] A. Winther and J. de Boer, Cal. Inst. Tech., Technical Report, 1965, p. 303.
[43] B. Harmatz, Nucl. Data Sheets **26**, 281 (1979).